The Astrophysical Journal, 978:36 (10pp), 2025 January 01 https://doi.org/10.3847/1538-4357/ad8d5a

Diversity in Hydrogen-rich Envelope Mass of Type II Supernovae. II. SN 2023ixf as Explosion of Partially Stripped Intermediate Massive Star

Qiliang Fang[1], Takashi J. Moriya[1,2,3], Lucía Ferrari[4,5], Keiichi Maeda[6], Gaston Folatelli[4,5,7], Keila Y. Ertini[4,5], Hanindyo Kuncarayakti[8,9], Jennifer E. Andrews[10], and Tatsuya Matsumoto[6,11]
[1] National Astronomical Observatory of Japan, National Institutes of Natural Sciences, 2-21-1 Osawa, Mitaka, Tokyo 181-8588, Japan
[2] Graduate Institute for Advanced Studies, SOKENDAI, 2-21-1 Osawa, Mitaka, Tokyo 181-8588, Japan
[3] School of Physics and Astronomy, Monash University, Clayton, Victoria 3800, Australia
[4] Facultad de Ciencias Astronómicas y Geofísicas, Universidad Nacional de La Plata, Paseo del Bosque S/N, B1900FWA La Plata, Argentina
[5] Instituto de Astrofísica de La Plata (IALP), CCT-CONICET-UNLP, Paseo del Bosque S/N, B1900FWA, La Plata, Argentina
[6] Department of Astronomy, Kyoto University, Kitashirakawa-Oiwake-cho, Sakyo-ku, Kyoto 606-8502, Japan
[7] Kavli Institute for the Physics and Mathematics of the Universe (WPI), The University of Tokyo, Kashiwa 277-8583, Chiba, Japan
[8] Tuorla Observatory, Department of Physics and Astronomy, FI-20014 University of Turku, Turku, Finland
[9] Finnish Centre for Astronomy with ESO (FINCA), FI-20014 University of Turku, Turku, Finland
[10] Gemini Observatory/NSF's NOIRLab, 670 N. A'ohoku Place, Hilo, HI 96720, USA
[11] Hakubi Center, Kyoto University, Yoshida-honmachi, Sakyo-ku, Kyoto 606-8501, Japan
Received 2024 September 5; revised 2024 October 19; accepted 2024 October 29; published 2024 December 24

Abstract

SN 2023ixf is one of the most well-observed core-collapse supernovae in recent decades, yet there is inconsistency in the inferred zero-age main-sequence (ZAMS) mass $M_{\rm ZAMS}$ of its progenitor. Direct observations of the pre-supernova (SN) red supergiant (RSG) estimate $M_{\rm ZAMS}$ spanning widely from 11 to 18 $M_{\odot}$. Additional constraints, including the host environment and the pulsation of its progenitor RSG, suggest a massive progenitor with $M_{\rm ZAMS} > 17\,M_{\odot}$. However, the analysis of the SN properties, from light-curve modeling to late-phase spectroscopy, favors a relatively low-mass scenario ($M_{\rm ZAMS} < 15\,M_{\odot}$). In this work, we conduct a systematic analysis of SN 2023ixf, from the RSG progenitor, plateau phase light curve to late-phase spectroscopy. Using MESA+STELLA to simulate the RSG progenitor and their explosions, we find that a range of the RSG models having $M_{\rm ZAMS}$ that vary from 12 to 17.5 $M_{\odot}$ can reproduce its multiband light curves if the hydrogen-rich envelope mass and the explosion energy are allowed to vary. Using late-phase spectroscopy as an independent measurement, the oxygen line [O I] indicates an intermediate-massive progenitor ($M_{\rm ZAMS} \sim 16.0\,M_{\odot}$). By incorporating the velocity structure derived from the light-curve modeling into an axisymmetric model, we generated [O I] line profiles that are consistent with the [O I] line observed in late-phase spectroscopy of SN 2023ixf. Bringing these analyses together, we conclude that SN 2023ixf is the aspherical explosion of an intermediate-massive star ($M_{\rm ZAMS} = 15$–$16\,M_{\odot}$), with the hydrogen envelope being stripped to 4–5 $M_{\odot}$ prior to its explosion.

Unified Astronomy Thesaurus concepts: Type II supernovae (1731); Core-collapse supernovae (304); Supernova dynamics (1664); Red supergiant stars (1375)

1. Introduction

SN 2023ixf is a Type II supernovae (SNe II) discovered in the nearby galaxy M101 on 2023 May 19. After its discovery by K. Itagaki (2023), SN 2023ixf attracted the attention of the community, and extensive observations were conducted, including photometry and spectroscopy covering ultraviolet (UV), optical, and infrared (IR) bands. The explosion site was also observed by Hubble Space Telescope, Spitzer Space Telescope, and ground-based telescopes prior to the explosion. These observations confirm that the progenitor of SN 2023ixf is a dusty red supergiant (RSG), surrounded by confined circumstellar medium (CSM; E. Berger et al. 2023; K. A. Bostroem et al. 2023; P. Chandra et al. 2023; Y. Dong et al. 2023; B. W. Grefenstette et al. 2023; D. Hiramatsu et al. 2023; G. Hosseinzadeh et al. 2023; W. V. Jacobson-Galán et al. 2023; C. D. Kilpatrick et al. 2023; I. A. Mereminskiy et al. 2023; J. L. Pledger & M. M. Shara 2023; M. Yamanaka et al. 2023; N. Smith et al. 2023; R. S. Teja et al. 2023; G. Li et al. 2024; L. Martinez et al. 2024; J. M. M. Neustadt et al. 2024; S. Panjkov et al. 2024; C. L. Ransome et al. 2024; D. Xiang et al. 2024; E. A. Zimmerman et al. 2024).

Being one of the most well-observed SNe II, SN 2023ixf holds significant potential for testing modern theories of stellar evolution and core collapse. For this purpose, it is important to accurately measure the zero-age main-sequence (ZAMS) mass of its progenitor. However, the estimated $M_{\rm ZAMS}$ using different methods are inconsistent. Imaging of the progenitor prior to the explosion is one of the most direct methods to estimate $M_{\rm ZAMS}$, while the estimations based on different assumptions on the properties of the dust and the models differ significantly: 8–10 $M_{\odot}$ (J. L. Pledger & M. M. Shara 2023); $11 \pm 2\,M_{\odot}$ (C. D. Kilpatrick et al. 2023); 16.2–17.4 $M_{\odot}$ (Z. Niu et al. 2023); $17 \pm 4\,M_{\odot}$ (J. E. Jencson et al. 2023); 9–14 $M_{\odot}$ (J. M. M. Neustadt et al. 2024); $12^{+2}_{-1}\,M_{\odot}$ (D. Xiang et al. 2024); 12–14 $M_{\odot}$ (S. D. Van Dyk et al. 2024); 14–20 $M_{\odot}$ (C. L. Ransome et al. 2024); and $18.1^{+0.7}_{-1.4}\,M_{\odot}$ (Y. -J. Qin et al. 2024). The observations of the SN 2023ixf progenitor with the Spitzer Space Telescope and ground-based telescopes reveal mid-IR variability with a period of $\sim$ 1000 days. Making use of the period–luminosity relation of RSGs in M31 (M. D. Soraisam et al. 2018) and M. D. Soraisam et al. (2023) estimate $M_{\rm ZAMS}$ to be $20 \pm 4\,M_{\odot}$. Further, the analysis of the stellar

Table 1
Inferred ZAMS Mass of the Progenitor of SN 2023ixf in the Literature

Method	$M_{\rm ZAMS}$ ($M_\odot$)	References
Host environment	17–19	Z. Niu et al. (2023)
	~ 22	C. Liu et al. (2023)
pre-SN images	8–10	J. L. Pledger & M. M. Shara (2023)
	11 ± 2	C. D. Kilpatrick et al. (2023)
	16.2–17.4	Z. Niu et al. (2023)
	17 ± 4	J. E. Jencson et al. (2023)
	9–14	J. M. M. Neustadt et al. (2024)
	12^{+2}_{-1}	D. Xiang et al. (2024)
	12–14	S. D. Van Dyk et al. (2024)
	14–20	C. L. Ransome et al. (2024)
	$18.1^{+0.7}_{-1.4}$	Y. -J. Qin et al. (2024)
Pulsation	20 ± 4	M. D. Soraisam et al. (2023)
	17–21	B. Hsu et al. (2024)
Light curve	12	M. C. Bersten et al. (2024)
	10	T. J. Moriya & A. Singh (2024)
	10	A. Singh et al. (2024)
Nebular spectroscopy	<15	L. Ferrari et al. (2024)

population in the vicinity of the explosion site favors a massive progenitor, from $16.2 \sim 17.4\,M_\odot$ (Z. Niu et al. 2023) to around $22\,M_\odot$ (C. Liu et al. 2023).

Hydrodynamic and radiative transfer modeling of the expelled material (ejecta) after the explosion is another useful way to constrain the properties of the progenitor. M. C. Bersten et al. (2024) show that the plateau phase light curve can be well-fitted by the model with $M_{\rm ZAMS} = 12\,M_\odot$ and explosion energy $E = 1.2 \times 10^{51}$ erg (hereafter we refer to 1.0×10^{51} erg as 1.0 foe). The progenitor model with $M_{\rm ZAMS} = 15\,M_\odot$ cannot provide the right plateau duration and magnitude at the same time. T. J. Moriya & A. Singh (2024) and A. Singh et al. (2024) employ the RSG models from T. Sukhbold et al. (2016), and they also find the model with $M_{\rm ZAMS} = 10\,M_\odot$ and $E = 2.0$ foe best matches the light curve. The late-phase (nebular) spectroscopy, derived 250 days after the explosion, supports the relatively low-mass scenario: when the ejecta becomes transparent, the spectroscopy is dominated by forbidden emission lines. Among them, the [O I] line can be used to measure the oxygen mass in the ejecta and constrain $M_{\rm ZAMS}$ (C. Fransson & R. A. Chevalier 1989; A. Jerkstrand et al. 2012, 2014; Q. Fang et al. 2019, 2022; D. Hiramatsu et al. 2021). L. Ferrari et al. (2024) found that the oxygen yield of SN 2023ixf is consistent with $M_{\rm ZAMS} = 12$–$15\,M_\odot$.

Table 1 summarizes the inferred ZAMS mass of the progenitor of SN 2023ixf from different representative studies.

In this work, we aim to solve the inconsistency seen in pre-supernova (SN) images, light-curve modeling, and nebular spectroscopy by taking the uncertainty of pre-SN mass loss into consideration. In Section 2, we construct RSG models that have the same $T_{\rm eff}$ and L as the pre-SN images from C. D. Kilpatrick et al. (2023), S. D. Van Dyk et al. (2024), and Y.-J. Qin et al. (2024), using the code Modules for Experiments in Stellar Astrophysics (MESA). The hydrogen-rich envelope of these RSG models is then artificially removed to mimic binary interaction or late stellar activities that may induce strong mass loss. The partial removal of the hydrogen-rich envelope hardly changes their positions on the Hertzsprung–Russell (H-R) diagram but can significantly affect the resulting light curves. The progenitor models are then used as the input of MESA +STELLA to trigger SN explosions and the radiative transfer modeling of the light curves. In Section 3, the model light curves are compared with the observational data of SN 2023ixf, which reveals that progenitor models with $M_{\rm ZAMS}$ even larger than $15\,M_\odot$ can produce light curves that closely match with observation if their hydrogen-rich envelopes are partially removed to $\sim 4\,M_\odot$. Light-curve modeling therefore cannot constrain $M_{\rm ZAMS}$ without knowing the amount of the hydrogen-rich envelope (L. Dessart & D. J. Hillier 2019; Q. Fang et al. 2024). In Section 4, we use nebular spectroscopy as an independent constraint on $M_{\rm ZAMS}$. By taking γ-photon leakage into consideration, we find evidence for an intermediate massive star ($M_{\rm ZAMS} \sim 16\,M_\odot$) and small hydrogen-rich envelope mass ($M_{\rm Henv} \lesssim 5\,M_\odot$). The double-peaked [O I] can be interpreted as an axisymmetric explosion. The conclusion is left to Section 5.

2. Numerical Setup

We use the one-dimensional stellar evolution code, MESA (B. Paxton et al. 2011, 2013, 2015, 2018, 2019; A. S. Jermyn et al. 2023) version r23.05.1 to simulate progenitor models with varied ZAMS mass, starting from the pre-main-sequence phase to the moment when the mass fraction of carbon $X_{\rm C}$ in the innermost cell drops below 10^{-3}. In this work, our light-curve analysis focuses on the plateau phase, which is not affected by late-stage evolution after core carbon depletion. We employ the mixing scheme similar to that of L. Martinez et al. (2020), i.e., Ledoux criterion for convection, exponential overshooting parameters $f_{\rm ov} = 0.004$ and $f_{\rm ov,0} = 0.001$ (the ratio of the amount of overshooting and the local pressure scale height), semiconvection efficiency $\alpha_{\rm sc} = 0.01$ (R. Farmer et al. 2016), and thermohaline mixing coefficient $\alpha_{\rm th} = 2$ (R. Kippenhahn et al. 1980). The reader may refer to the documents of MESA for the details of these parameters.[12]

The mixing length parameter $\alpha_{\rm mlt}$ (the ratio of the mixing length and the local pressure scale height) is varied to tune the effective temperature $T_{\rm eff}$ of the progenitors such that the RSG models match with pre-SN images on the H-R diagram at the endpoint of the calculation. Throughout the calculation, we ignore wind-driven mass loss. After core helium depletion, we turn on the command `relax_initial_mass_to_remove_H_env` and use `extra_mass_retained_by_remove_H_env` to artificially remove the hydrogen-rich envelope. The calculation is carried on until core carbon depletion without mass loss. The ZAMS mass range is selected to match with the progenitor luminosity, estimated from the pre-SN images of Y.-J. Qin et al. (2024) (high mass; 16.5–18.5 $M_\odot$), S. D. Van Dyk et al. (2024) (intermediate mass; 14.0–16.0 $M_\odot$), and C. D. Kilpatrick et al. (2023) (low mass; 11.5–13.0 $M_\odot$).[13]

Here, our ZAMS mass estimation is slightly higher than S. D. Van Dyk et al. (2024), where the ZAMS mass is proposed to be $12.0 \sim 14.0\,M_\odot$. This is because compared with their reference models, given the same ZAMS mass, our models have smaller helium cores and appear to be fainter on the H-R diagram. However, we do not attempt to change $f_{\rm ov}$, a key

[12] https://docs.mesastar.org/en/23.05.1/index.html

[13] Although J. L. Pledger & M. M. Shara (2023) derive an $M_{\rm ZAMS}$ of 8–10 $M_\odot$, MESA encounters numerical difficulties within this mass range. In this work, we adopt a slightly higher $M_{\rm ZAMS}$ value from C. D. Kilpatrick et al. (2023) as a representative estimate for lower-mass progenitors.

parameter that controls the helium core mass for fixed ZAMS mass (see, for example, D. Temaj et al. 2024), to align our ZAMS mass estimation because the progenitor models in this work follow the same $M_{\rm ZAMS}$–$M_{\rm He\ core}$ relation as that of T. Sukhbold et al. (2016), which is frequently used as the initial models for core-collapse simulation (A. Burrows & D. Vartanyan 2021) and nebular spectroscopy modeling, which will be discussed in later sections. It is the helium core mass (or more precisely, the carbon-oxygen core mass), rather than the ZAMS mass that determines the amount of oxygen element and the core-collapse process. Throughout this work, the estimation of ZAMS mass is based on these progenitor models that follow a fixed $M_{\rm ZAMS}$–$M_{\rm He\ core}$ relation (Figure 1).

We further note that $T_{\rm eff}$ from S. D. Van Dyk et al. (2024), estimated to be 2770 K, is too cool to be reproduced by the RSG models in this work; we therefore adopt $T_{\rm eff} = 3110 \sim 3330$ K, which are the lower and upper values of $T_{\rm eff}$ of IRC-10414, a Galactic RSG analog of the SN 2023ixf progenitor (V. V. Gvaramadze et al. 2014; M. Messineo & A. G. A. Brown 2019; S. D. Van Dyk et al. 2024).

After core carbon depletion, we closely follow the test suite `ccsn_IIp` to trigger the explosion of the progenitor model with varied explosion energy $E_{\rm K}$. After the shock wave has reached 0.05 $M_\odot$ below the stellar surface, we artificially deposit 0.06 $M_\odot$ ^{56}Ni uniformly in the helium core ($M_{\rm Ni}$ is taken from A. Singh et al. 2024 and T. J. Moriya & A. Singh 2024), and use a boxcar scheme to smooth the abundance profiles in the ejecta (D. Kasen & S. E. Woosley 2009; L. Dessart et al. 2012, 2013; V. Morozova et al. 2015; Q. Fang et al. 2024). The model is then handed off to `STELLA` for the calculation of the light curve. A detailed description of this workflow can be found in the literature (B. Paxton et al. 2018; J. A. Goldberg et al. 2019; D. Hiramatsu et al. 2021; Q. Fang et al. 2024).

The parameters of the RSG progenitor models are listed in Table 2. The comparison of the models and the RSG progenitors of SN 2023ixf from pre-SN images on the H-R diagram is shown in Figure 1. The `MESA` inlists used to generate the models in the work are available on Zenodo under an open-source Creative Commons Attribution 4.0 International license: doi:10.5281/zenodo.13953755.

3. Light-curve Analysis

The photometry data of SN 2023ixf in the *BgVriz* bands are collected from A. Singh et al. (2024), and the reader may refer to that paper for the details of the observation setup. Here, we adopt the distance of 6.85 ± 0.15 Mpc (A. G. Riess et al. 2022) and total extinction of $E(B-V) = 0.039$ mag (E. F. Schlafly & D. P. Finkbeiner 2011; M. Lundquist et al. 2023) with $R_V = 3.1$. Extinctions in different bands are estimated from the extinction law of J. A. Cardelli et al. (1989).

The light curve of SN 2023ixf is characterized by a rapid rise to $M_V \sim -18.4$ mag, followed by a gradual decline to a plateau at $M_V \sim -17.6$ mag. The early-phase emission indicates the presence of dense CSM that is not predicted by standard stellar evolution theory[14] (B. W. Grefenstette et al. 2023; D. Hiramatsu et al. 2023; G. Hosseinzadeh et al. 2023; W. V. Jacobson-Galán et al. 2023; N. Smith et al. 2023; R. S. Teja et al. 2023; M. Yamanaka et al. 2023; L. Martinez et al. 2024; E. A. Zimmerman et al. 2024) whose properties have been extensively studied (see, for example, D. Hiramatsu et al. 2023; L. Martinez et al. 2024; A. Singh et al. 2024; E. A. Zimmerman et al. 2024). While the CSM around SN 2023ixf is crucial for understanding stellar evolution, it is not the focus of this work. As pointed out by V. Morozova et al. (2018) and T. Moriya et al. (2011), CSM interaction dominates

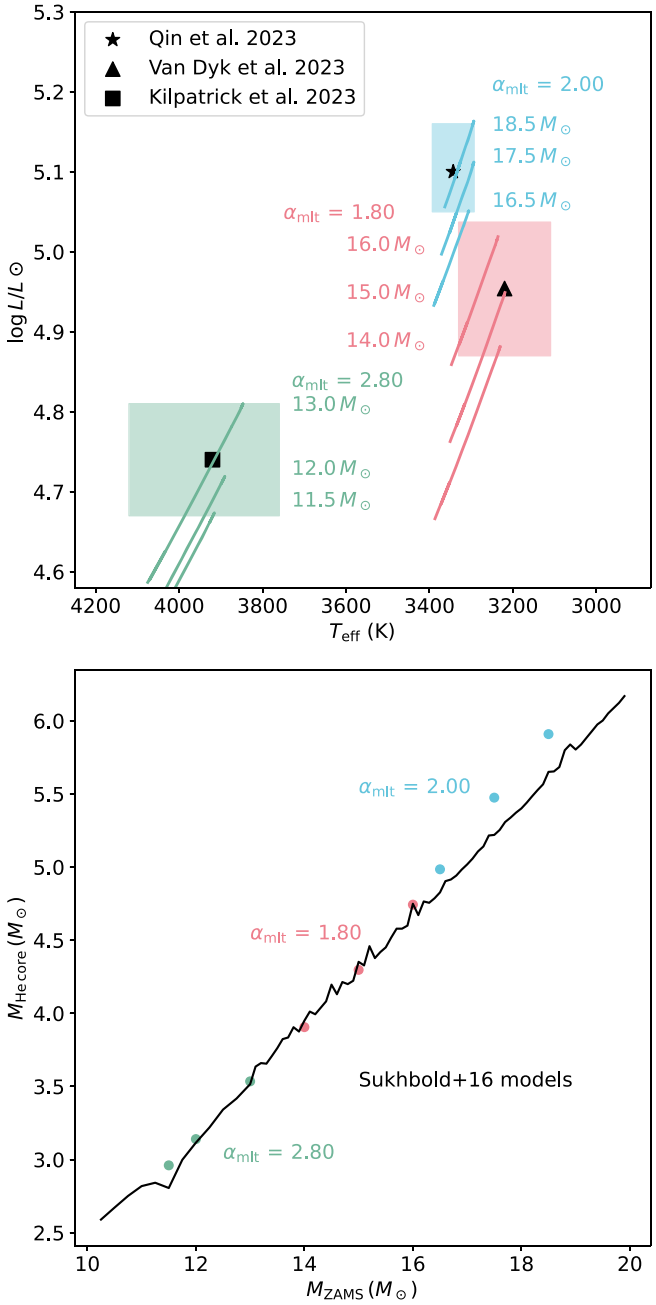

Figure 1. Upper panel: the comparison of the models and the RSG progenitors of SN 2023ixf from pre-SN images on the H-R diagram. The filled black star, triangle, and square are the measurements of S. D. Van Dyk et al. (2024), Y. -J. Qin et al. (2024), and C. D. Kilpatrick et al. (2023), which represent the high-mass, intermediate-mass, and low-mass estimations for the SN 2023ixf progenitor. The shaded regions are the corresponding uncertainties. The color lines are the evolution tracks of some representative progenitor models at the carbon-burning phase. Lower panel: the $M_{\rm ZAMS} - M_{\rm He\ core}$ relation in this work. The black line represents the models from T. Sukhbold et al. (2016).

[14] J. Fuller & D. Tsuna (2024) proposed an alternative scenario where dense chromospheric material between the stellar surface and the dust formation radius can explain the initial rise in the light curve, as well as the rapid disappearance of the flash ionization features, without introducing a large amount of CSM. This scenario is consistent with the lack of observed precursors reported by Y. Dong et al. (2023), J. M. M. Neustadt et al. (2024), and C. L. Ransome et al. (2024).

Table 2
Progenitor Models in This Work

RSG Progenitor	$T_{\rm eff}$ (K)	$\log L/L_{\odot}$	$\alpha_{\rm mlt}$	$M_{\rm ZAMS}$ ($M_{\odot}$)	$M_{\rm Henv}$ ($M_{\odot}$)	$M_{\rm rem}$ ($M_{\odot}$)	$E_{\rm K}$ (foe)
Y.-J. Qin et al. (2024)	3343^{+50}_{-50}	$5.10^{+0.05}_{-0.05}$	2.00	17.5	3.0–7.5	1.8	0.5–1.5
S. D. Van Dyk et al. (2024)	3220^{+110}_{-110}	$4.95^{+0.09}_{-0.08}$	1.80	15.0	3.0–7.5	1.8	0.5–1.5
C. D. Kilpatrick et al. (2023)	3920^{+200}_{-160}	$4.74^{+0.07}_{-0.07}$	2.80	12.0	3.0–8.0	1.5	1.0–2.5

early-phase observations. In this scenario, the CSM is located very close to the stellar surface and is rapidly swept up, resulting in minimal effects on the light-curve plateau, especially in the *gVriz* bands. The plateau duration and magnitude are mainly affected by the explosion energy ($E_{\rm K}$) and the ejecta mass ($M_{\rm eje}$). Therefore, we do not include CSM in our models to avoid introducing unrelated parameters. Our analysis is restricted to $t > 40$ days, i.e., after the midpoint of the plateau.

For progenitor models with the same $M_{\rm ZAMS}$, we use $M_{\rm Henv}$ and $E_{\rm K}$ as free parameters to fit the multiband light curves of SN 2023ixf. Because our models do not include CSM, the initial rapid rise in the light curve is not reproduced. The qualities of the fits are evaluated from $t > 40$ days, covering roughly from the midpoint of the plateau to the onset of the radioactive tail. The ranges of $M_{\rm Henv}$ and $E_{\rm K}$ are listed in Table 2, with steps of 0.25 $M_{\odot}$ 0.1 foe, respectively. The best-fit model is determined by interpolating the model light curves to the observed epochs in the different bands and minimizing χ^2. The photosphere velocities, estimated from the Fe II absorption minimum in early-phase spectroscopy, measured in A. Singh et al. (2024), are not included in the fitting process, but used as independent evaluations of the qualities of the fits. The results of the best-fit parameters to models with $M_{\rm ZAMS} = 17.5\,M_{\odot}$ (Y.-J. Qin et al. 2024), $15.0\,M_{\odot}$ (S. D. Van Dyk et al. 2024), and $12.0\,M_{\odot}$ (C. D. Kilpatrick et al. 2023) are shown in Figure 2.

From the results of light-curve modeling, we conclude that, if $M_{\rm Henv}$ is allowed to vary, RSG progenitors with $M_{\rm ZAMS}$ as massive as 15–18 $M_{\odot}$ can produce similar light curves to those of relatively low-mass progenitors ($M_{\rm ZAMS} \sim 12\,M_{\odot}$) with almost all of their hydrogen-rich envelopes attached. The artificial removal of the hydrogen-rich envelope does not significantly change the stellar radius as long as the residual $M_{\rm Henv}$ remains larger than $\sim 3\,M_{\odot}$ (see Table 2 of V. Morozova et al. 2015 or Figure 1 of Q. Fang et al. 2024). The luminosity, primarily determined by the helium core mass, is also unaffected by this process. Therefore, partial removal of the hydrogen-rich envelope does not alter the position of the progenitor RSG on the H-R diagram, aligning with results from pre-SN images, while it introduces diversity in light-curve properties. Without knowing the mass of the residual hydrogen-rich envelope, which can be significantly influenced by the presence of a companion star or complex eruptive activity in the late phases of massive star evolution, light-curve modeling cannot determine the $M_{\rm ZAMS}$ of the SN progenitor. For this purpose, another independent measurement is required.

4. Nebular Spectroscopy Analysis

While the light curve during the plateau phase is largely affected by the mass of the hydrogen-rich envelope and is therefore sensitive to the uncertain mass-loss history prior to the explosion, late-phase (nebular phase) spectroscopy, taken several months to a year after the explosion when the ejecta becomes optically thin, is primarily determined by the properties of the innermost core. At this phase, the spectroscopy of the SN is dominated by emission lines, with particularly strong lines being [O I] $\lambda\lambda$ 6300,6363, Hα and [Ca II] $\lambda\lambda$ 7291,7323. The absolute or relative flux of [O I] is an useful proxy of the amount of the oxygen elements in the core region, therefore is frequently employed as the indicator of the ZAMS mass of the progenitor from aspects of both theory and observation. In this section, we conduct an analysis of the nebular spectroscopy of SN 2023ixf, taken at $t = 259$ days after the explosion. The reader may refer to L. Ferrari et al. (2024) for the observation setup.

4.1. [O I] Luminosity

In L. Ferrari et al. (2024), based on nebular spectroscopy analysis, the ZAMS mass of the progenitor of SN 2023ixf is proposed to be 12–15 $M_{\odot}$, consistent with the pre-SN images of C. D. Kilpatrick et al. (2023) and S. D. Van Dyk et al. (2024). The conclusion is made based on several lines of evidence: (1) when scaled to the same distance, the [O I] flux of SN 2023ixf is relatively low compared with model spectroscopy at a similar phase taken from A. Jerkstrand et al. (2012) and A. Jerkstrand et al. (2014); (2) The [O I]/[Ca II] ratio, which is a useful proxy of the progenitor CO core mass, is as low as 0.51, falling between the models with $M_{\rm ZAMS} = 12\,M_{\odot}$ and $M_{\rm ZAMS} = 15\,M_{\odot}$.

While these arguments are well-supported by direct comparison with model spectroscopy, they may not fully apply to SN 2023ixf. The models employed for comparison assume massive hydrogen-rich envelopes and have been found to match well with the observations of SNe 2004et and 2012aw, which have a long plateau of ~120 days. In contrast, the plateau duration of SN 2023ixf is ~80 days (M. C. Bersten et al. 2024), approximately 40 days shorter, meaning it enters the nebular phase earlier. Additionally, the radioactive tail of SN 2023ixf declines faster than those of SNe 2004et and 2012aw. These two factors make SN 2023ixf appear ~0.8 mag fainter in the *R* band than the model spectroscopy, suggesting that the low [O I] luminosity of SN 2023ixf does not necessarily indicate a low oxygen abundance compared with model progenitors. Instead, it is likely a result of a lower fraction of γ-photons, emitted from the radioactive decay of ^{56}Co, being trapped in the ejecta.

In Figure 3, we compare the model spectroscopy from A. Jerkstrand et al. (2012) and A. Jerkstrand et al. (2014) with SN 2023ixf, normalizing all spectra to the integrated fluxes from 4500 to 8000 Å. This normalization ensures that the models and SN 2023ixf have the same amount of deposited radioactive energy in this wavelength range. Consequently, the fractional flux of the emission lines reflects the relative abundance of the emitting elements in the line-forming region. SN 2023ixf shows apparently stronger [O I] emission than the

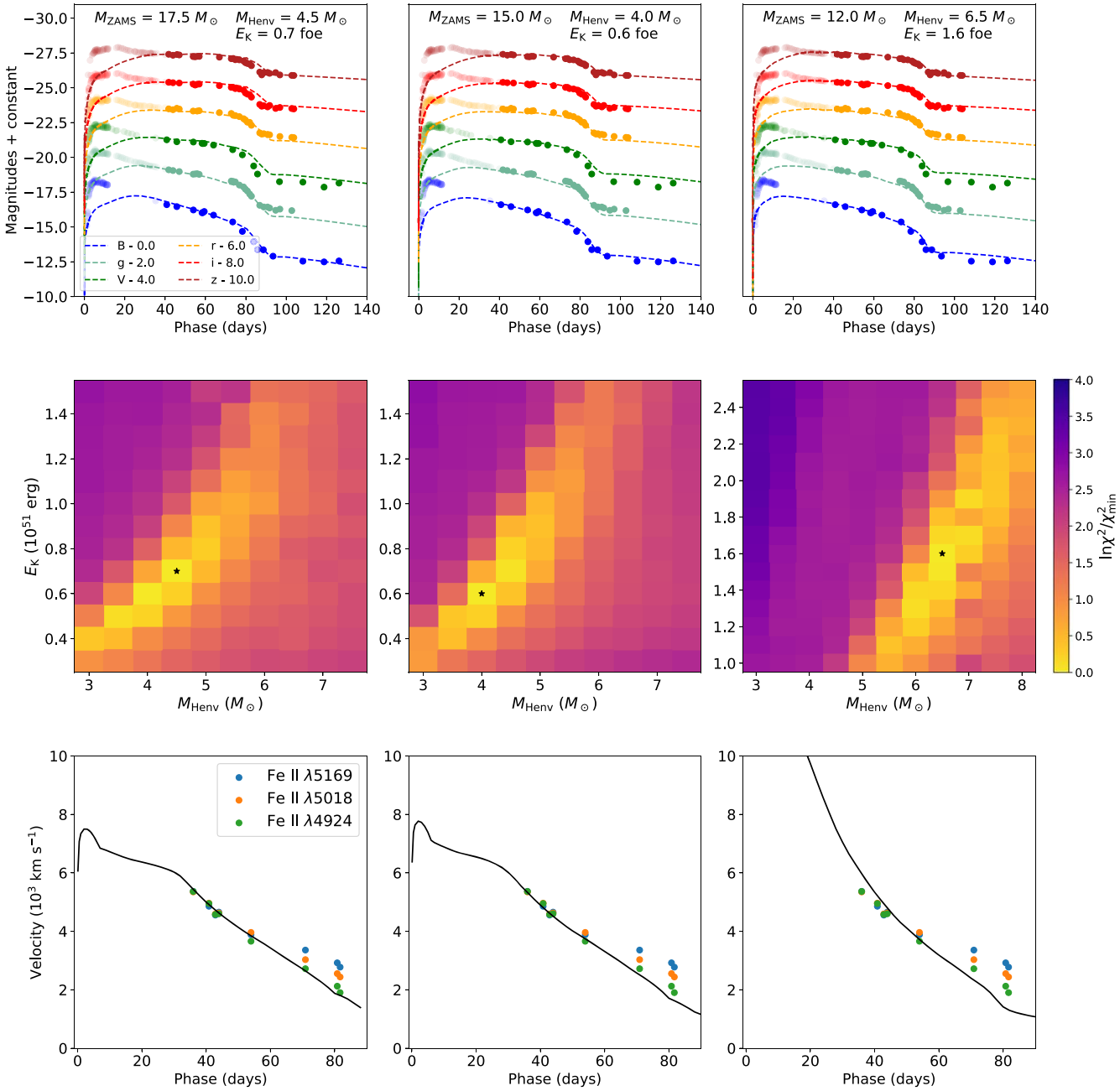

Figure 2. Upper panels: the light curves of the best-fit M_{Henv} and E_K for models with $M_{ZAMS} = 17.5\,M_\odot$ (left; Y.-J. Qin et al. 2024), $M_{ZAMS} = 15.0\,M_\odot$ (middle; S. D. Van Dyk et al. 2024), and $M_{ZAMS} = 12.0\,M_\odot$ (right; C. D. Kilpatrick et al. 2023). The photometry of SN 2023ixf are the scatter points, and data from different filters are labeled by different colors. The solid points are used for fitting. The dotted lines represent the light curves of the best-fit models. Middle panels: color-coded ratio of χ^2 to χ^2_{min} at the M_{Henv}–E_K space. The filled black star marks the parameter pair (M_{Henv}, E_K) with the minimum χ^2. The color bar is floored at $\ln \chi^2/\chi^2_{min} = 4.0$. Lower panels: the evolution of the photospheric velocities of SN 2023ixf (scatter points) and the best-fit models (black lines).

models with $M_{ZAMS} = 12\,M_\odot$ (hereafter referred to as the M12 model, respectively; similarly, M15, M19, and M25 refer to the models with $M_{ZAMS} = 15$, 19, and $25\,M_\odot$), while its flux is between the M15 and M19 models. The fractional [O I] fluxes of the models, as a function of ZAMS masses, are compared with that of SN 2023ixf in Figure 3. Direct interpolation gives $M_{ZAMS} \sim 16.3\,M_\odot$ for SN 2023ixf, close to the upper limit of S. D. Van Dyk et al. (2024) and the lower limit of Y.-J. Qin et al. (2024).

The above analysis is based on the assumption that the γ-photon escape probability is the same throughout the ejecta, from the dense carbon-oxygen core to the hydrogen-rich envelope. In this case, decreasing the total luminosity by 60% (0.8 mag in the R band) will at the same time decrease the [O I] luminosity by the same amount; therefore, the fractional flux of [O I] remains unchanged and can be used to determine M_{ZAMS}. In practice, this assumption does not hold as γ-photons can more easily escape from the outermost envelope. Here, we consider an extreme case, i.e., all the additional leakage of γ-photons are originally radiated in the form of Hα from the envelope, and the relatively low luminosity of SN 2023ixf, compared with the models with their hydrogen-rich envelope fully attached, is attributed to the weak Hα emission, while other spectral lines remain unaffected. The oxygen fluxes of the models and SN 2023ixf are then accordingly normalized to the integrated fluxes without Hα line, i.e., we only consider the

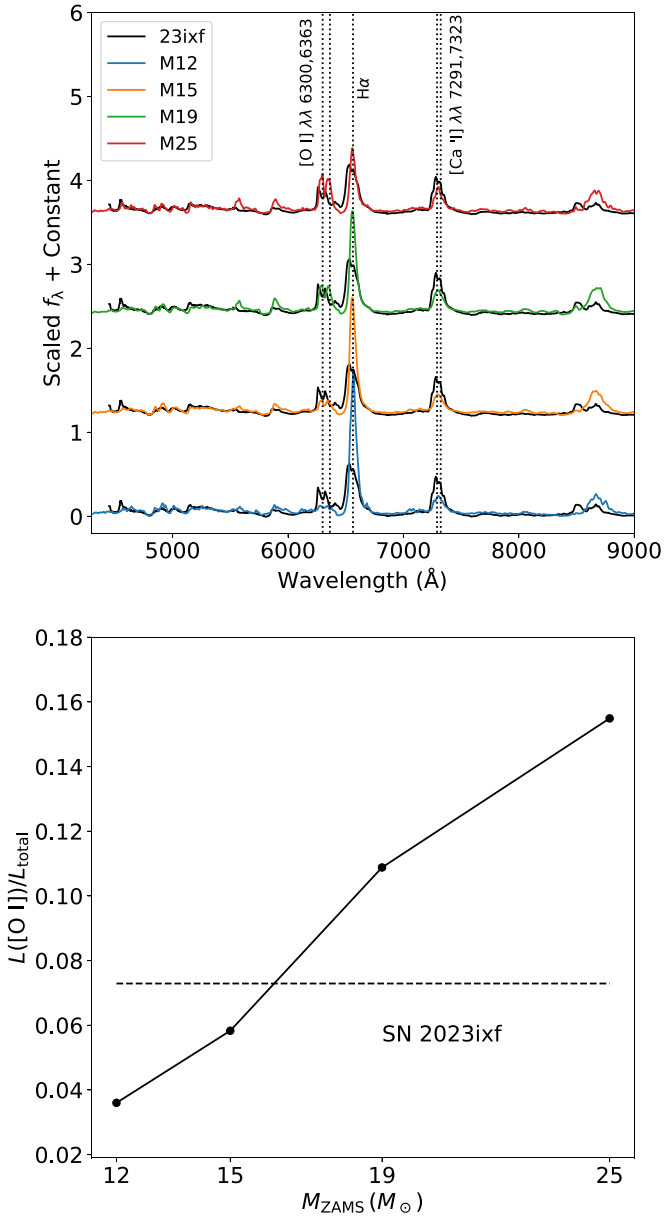

Figure 3. Upper panel: the comparison of the spectroscopy models at 250 days, taken from A. Jerkstrand et al. (2012) and A. Jerkstrand et al. (2014), with the nebular spectrum of SN 2023ixf from L. Ferrari et al. (2024). All spectra are normalized to the integrated flux from 4500 to 8000 Å. Lower panel: the fractional flux of [O I] as a function of $M_{\rm ZAMS}$. The dashed line indicates the measurement for SN 2023ixf.

integrated fluxes of the metal emission lines. Similar to the above analysis, interpolation gives $M_{\rm ZAMS} \sim 15.2\,M_\odot$. Our final estimation of $M_{\rm ZAMS}$ based on nebular spectroscopy therefore falls between 15.2 to 16.3 $M_\odot$.

While the [O I] flux of SN 2023ixf is within the range of the M12 to M25 models, its Hα emission is noticeably weaker. Given the same total energy, the [O I] flux of SN 2023ixf is about half the value observed in the M15 and M19 models. Although the formation of Hα is complex and influenced by many processes, such as mixing, its relative weakness compared to models with a massive hydrogen-rich envelope qualitatively supports the idea that the hydrogen-rich envelope of SN 2023ixf is partially removed. The interpretation here is limited by our current lack of nebular spectroscopy models for partially stripped SNe IIP; however, a pioneering study by L. Dessart & D. J. Hillier (2020) shows that for SNe IIP with low-mass hydrogen-rich envelopes, the [O I] line is not significantly affected, while the fluxes of Hα dramatically decrease and [Ca II] slightly increase (see their Figure 9). This behavior is roughly consistent with the observations of SN 2023ixf, and explains the relatively low [O I]/[Ca II] compared with the M15 model (L. Ferrari et al. 2024).

In conclusion, nebular spectroscopy analysis supports the hypothesis that SN 2023ixf is the explosion of an RSG of $M_{\rm ZAMS} \sim 15.2$–$16.3\,M_\odot$, similar to the estimation of S. D. Van Dyk et al. (2024), with $M_{\rm Henv} \lessapprox 5\,M_\odot$ (about half the values of M15 and M19 models), which is much lower than the prediction of single stellar models evolved with standard stellar wind (T. Sukhbold et al. 2016; Q. Fang et al. 2024).

4.2. Emission Line Profiles

During the nebular phase, the ejecta expands homologously, i.e., the radial expansion velocity of a fluid parcel is proportional to its radial coordinate. Additionally, the emission line widths are dominated by Doppler broadening, therefore directly reflecting the spatial distributions of the emitting elements. Consequently, the emission lines observed in nebular spectroscopy provide information not only on the abundance of different elements but also on their geometric distributions within the ejecta (S. Taubenberger et al. 2009; A. Jerkstrand 2017; Q. Fang et al. 2022; B. F. A. van Baal et al. 2023).

In this work, we focus on the profile of the [O I] line. The [O I] line exhibits a horn-like (or double-peak) profile (L. Ferrari et al. 2024; A. Singh et al. 2024), characterized by a trough located at $v \sim 0\,{\rm km\,s^{-1}}$, with symmetric blue- and redshifted peaks around it. While double-peaked [O I] is frequently observed in stripped-envelope supernova (SESN; core-collapse SNe that have lost almost all of their hydrogen-rich envelope prior to the explosions; see P. A. Mazzali et al. 2005; K. Maeda et al. 2008; M. Modjaz et al. 2008; S. Taubenberger et al. 2009; D. Milisavljevic et al. 2010; Q. Fang et al. 2022), it is rarely seen for the emission lines of hydrogen-rich SNe (with few exceptions; see, for example, N. N. Chugai et al. 2005; J. E. Andrews et al. 2019; V. P. Utrobin & N. N. Chugai 2019; V. P. Utrobin et al. 2021), although the signature of asphericity can be detected from spectropolarimetry (D. C. Leonard & A. V. Filippenko 2001; D. C. Leonard et al. 2006; L. Wang & J. C. Wheeler 2008; B. Kumar et al. 2016; T. Nagao et al. 2019; S. S. Vasylyev et al. 2023, 2024; T. Nagao et al. 2024, 2024).[15] This peculiar profile is interpreted as emission from an oxygen-rich torus surrounding a bipolar calcium-rich region, being viewed from the edge (K. Maeda et al. 2002, 2006, 2008; Q. Fang et al. 2022, 2024).

Here, we use the velocity profile from the models that best fit the light curves in Section 3 to synthesize the [O I] line profile with the axisymmetric model proposed in Q. Fang et al. (2024). The model is characterized by an oxygen-rich ball excised by two detached ellipsoids, within which all the oxygen elements are burnt into heavy elements (see Figure 4; blue region: oxygen-rich unburnt material with oxygen mass fraction $X_{\rm O} = 1$; red region: explosive burning ash with $X_{\rm O} = 0$). We further assume that the material in the helium core, including the oxygen-rich region, is fully mixed (A. Jerkstrand et al. 2012). Consequently, the boundary velocity of the oxygen-

[15] Recently, the spectropolarimetry of SN 2023ixf was reported by A. Singh et al. (2024) and M. Shrestha et al. (2024), which shows evidence of asphericity in the helium core.

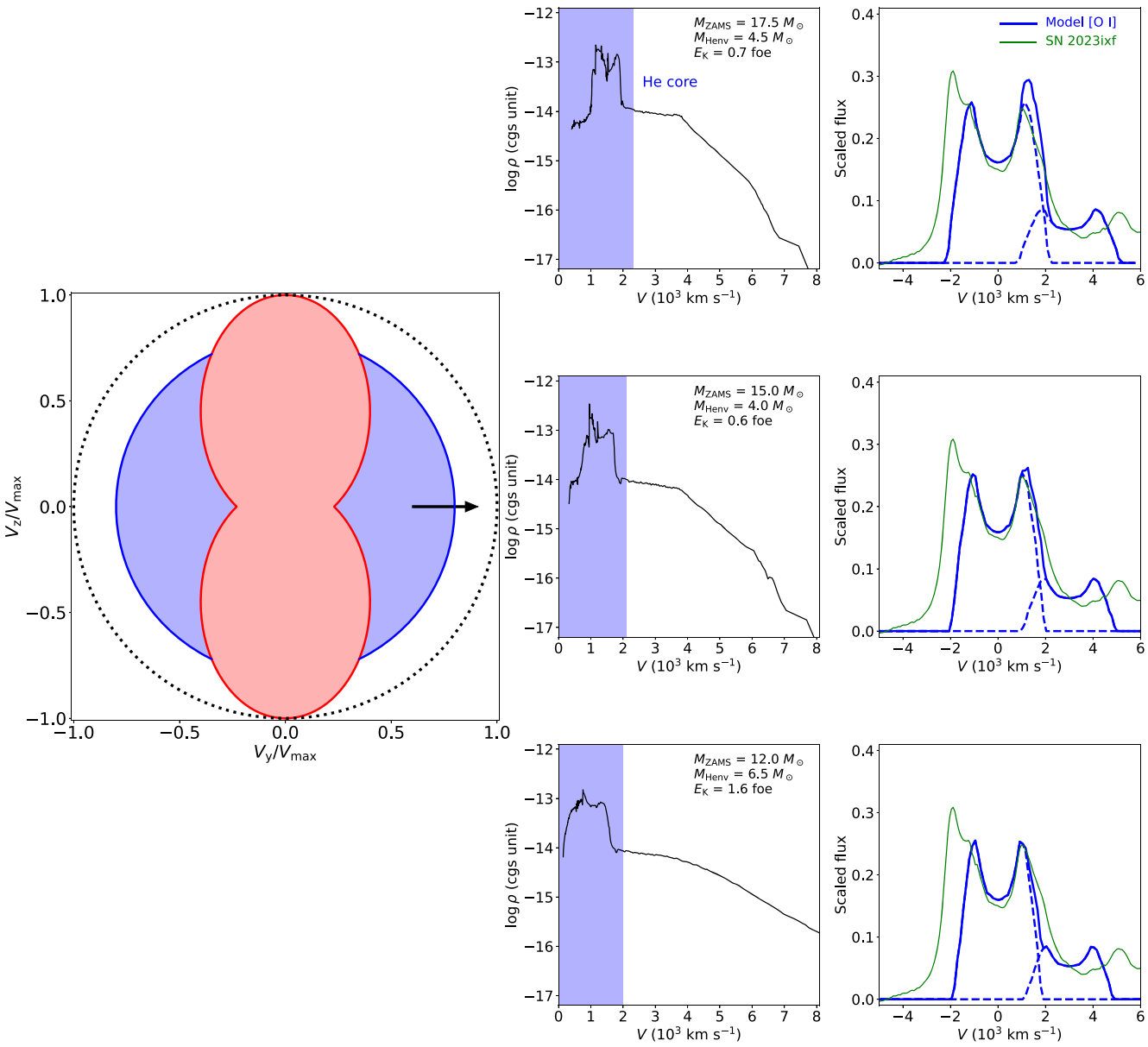

Figure 4. The bipolar structure of the ejecta and the synthesized [O I] line. Left panel: the axisymmetric bipolar ejecta model proposed in Q. Fang et al. (2024). The red-shaded region is the explosive burning ash, containing only iron-peak elements. The blue-shaded region is the oxygen-rich material from which [O I] is emitted. Middle panels: the density structure of the ejecta of the best-fit models for light-curve modeling (Section 3 and Figure 2), as a function of the velocity coordinate. The blue-shaded regions represent the helium cores. Right panels: comparison between the observed [O I] profile of SN 2023ixf (green line) with the synthesized [O I] profile (blue line). The blue-dashed lines are the two components of [O I] centering at 6300 and 6363 Å, respectively. The ratio of their intensities is assumed to be 3:1. From top to bottom: $M_{\rm ZAMS} = 17.5\,M_\odot$ (Y.-J. Qin et al. 2024), $M_{\rm ZAMS} = 15.0\,M_\odot$ (S. D. Van Dyk et al. 2024), and $M_{\rm ZAMS} = 12.0\,M_\odot$ (C. D. Kilpatrick et al. 2023).

emitting region, $V_{\rm O}$, is the same as the velocity at the edge of the helium core, and the density in this region is a constant. Using the procedure outlined in Q. Fang et al. (2024), the synthesized [O I] profiles, viewed from $\theta = 90°$, are shown in Figure 4. For all the models, despite variations in $M_{\rm ZAMS}$, $M_{\rm Henv}$, and $E_{\rm K}$, the synthesized [O I] profiles align well with observation[16]). This consistency indicates that the horn-like profile of [O I] indeed originates from the oxygen-rich torus. Additionally, the [O I] line width of SN 2023ixf also requires the material in the helium core to be fully mixed: if we use the velocity at the edge of the carbon-oxygen core, which is about 1000–1500 km s^{-1}, to model the [O I] line, the synthesized [O I] lines are extremely narrow and none of the profiles provide a satisfactory match with the observation.

The analysis in this section is based on the assumption that the double-peak [O I] profile results from a geometrical effect of the ejecta. Nevertheless, unlike SESN where the separation of the two peaks is wide (see Q. Fang et al. 2024), for SN 2023ixf, the separation is ∼3000 km s^{-1}, i.e., close to that of the two components of the [O I] doublet. We, therefore, cannot reject other possibilities, such as clumping (H. Kuncarayakti et al. 2020; L. Ferrari et al. 2024) or a unipolar oxygen-rich

[16] We notice that the synthesized line profile is narrower than the observed one, especially in the blue wing. However, this difference can be resolved if we allow the oxygen-rich material, originally in the helium core, to mix slightly outward. We further note that the model is very simplified without considering radiative transfer effects. This may also contribute to the lack of flux in the blue wing

blob moving toward the observer (S. Taubenberger et al. 2009; D. Milisavljevic et al. 2010), accelerated by neutron star kick (see, for example, A. Burrows et al. 2024). Distinguishing these scenarios from a bipolar explosion in an individual SN is challenging (S. Taubenberger et al. 2009; Q. Fang et al. 2022). However, from a statistical perspective, such scenarios would require that some SNe II exhibit a horn-like [O I] profile with both peaks redshifted, which, to our knowledge, has not yet been observed. Q. Fang et al. (2022) conducted a statistical study of the nebular spectra of 103 SESNe and concluded that the unipolar blob scenario is not favored if the absolute wavelength shift of the narrow component exceeds $1500\,\mathrm{km\,s^{-1}}$, due to the imbalance in the numbers of objects with their narrow [O I] peaks red- and blueshifted (see Section 6.3 of Q. Fang et al. 2022). In the case of SN 2023ixf, this shift is $1700\,\mathrm{km\,s^{-1}}$ (L. Ferrari et al. 2024). Based on these considerations, we find a bipolar explosion with a torus-like structure to be the more plausible interpretation from a statistical viewpoint, while alternative scenarios, such as clumping or a unipolar blob, still cannot be ruled out for an individual object like SN 2023ixf.

5. Conclusion

SN 2023ixf is one of the most well-observed core-collapse SNe in recent decades, yet there is large scatter in the $M_{\rm ZAMS}$ of its progenitor inferred from pre-SN images. This inconsistency may partly be attributed to the different assumptions on the complicated dusty environment (see the discussion in S. D. Van Dyk et al. 2024). In this work, we attempt to estimate $M_{\rm ZAMS}$ from the SN explosion itself. For this purpose, we construct RSG models that occupy the same position on the H-R diagram as the proposed progenitor of SN 2023ixf, based on the pre-explosion images from C. D. Kilpatrick et al. (2023), S. D. Van Dyk et al. (2024), and Y.-J. Qin et al. (2024). From these progenitor models, we artificially remove their hydrogen-rich envelope and trigger explosions, and compare the resulting light curves with the multiband photometry of SN 2023ixf. Our findings indicate that, by varying the hydrogen envelope mass $M_{\rm Henv}$ and explosion energy $E_{\rm K}$, RSG models with $M_{\rm ZAMS}$ ranging from 12.5 to $17.5\,M_{\odot}$ can produce light curves that closely match the observed data. Consequently, light-curve modeling alone cannot effectively constrain $M_{\rm ZAMS}$ due to this degeneracy.

To address this limitation, we employ nebular spectroscopy as an independent method for estimating $M_{\rm ZAMS}$. The fractional flux of the [O I] line suggests $M_{\rm ZAMS}$ values between 15.2 and $16.3\,M_{\odot}$. Interestingly, the Hα line also provides additional constraints: an RSG model with $M_{\rm ZAMS} = 12.0\,M_{\odot}$ must retain a massive hydrogen envelope ($M_{\rm Henv} = 6.5\,M_{\odot}$) to match the plateau light curve. However, this is inconsistent with the weak Hα line observed in the nebular phase, implying that a large fraction of the hydrogen-rich envelope was removed prior to the explosion, as suggested by the light-curve modeling results for RSG models with $M_{\rm ZAMS} = 15.0$ and $17.5\,M_{\odot}$.

Finally, we employed the axisymmetric ejecta structure from Q. Fang et al. (2024) to model the [O I] line profile of SN 2023ixf. By assuming the maximum velocity of the [O I] emitting region corresponds to the edge velocity of the helium core, taken from the velocity profiles of models that best fit the observed plateau light curve, we achieve satisfactory matches between the observed double-peaked [O I] of SN 2023ixf and the synthesized [O I] profiles, viewed from 90°. This agreement not only confirms the aspherical nature of the explosion, but also provides additional constraints on material mixing: the helium core material, including oxygen-rich regions, must be thoroughly mixed to account for the relatively broad [O I] profile observed in the nebular phase.

Bringing these lines of evidence together, we propose that SN 2023ixf represents the aspherical explosion of a partially stripped, intermediate-mass RSG with $M_{\rm ZAMS}$ between 15.3 and $16.2\,M_{\odot}$. We further note that stars within this mass range do not have the strong stellar winds necessary to strip their hydrogen-rich envelope to this small amount. Other mechanisms, such as binary interaction (see, for example, A. Ercolino et al. 2024 for a recent study), pulsation-driven mass loss (see S.-C. Yoon & M. Cantiello 2010; J. A. Goldberg et al. 2020), among other potential candidates, must be involved to assist the removal of a significant fraction of the hydrogen-rich envelope.

Our inferred $M_{\rm ZAMS}$ for the SN 2023ixf progenitor, based on the nebular spectroscopy, is lower than the estimation derived from the RSG pulsation period ($20 \pm 4\,M_{\odot}$; M. D. Soraisam et al. 2023). In M. D. Soraisam et al. (2023), they first measure the period of the progenitor's light curve, and infer the K-band magnitude from the magnitude–period relation of RSGs reported in M. D. Soraisam et al. (2018). The bolometric luminosity is then calculated by applying the bolometric correction from E. M. Levesque et al. (2005). However, as S. D. Van Dyk et al. (2024) pointed out, the majority of the star's flux emerges in the IR band, and applying the bolometric correction from E. M. Levesque et al. (2005) may lead to an overestimation of both the total luminosity and $M_{\rm ZAMS}$. Additionally, Z. Niu et al. (2023) also report a slightly larger $M_{\rm ZAMS}$ range (17–$19\,M_{\odot}$) inferred from the ages of the young stellar populations near the explosion site. However, Z. Niu et al. (2023) assume single-aged populations, while in reality, star formation can occur sequentially. Assuming that the progenitor of SN 2023ixf is coeval with the youngest population could lead to an overestimate of its $M_{\rm ZAMS}$, and thus, this mass range should be regarded as an upper limit (see the discussion in N.-C. Sun et al. 2021). In light of these considerations, our inferred $M_{\rm ZAMS}$ does not conflict with the estimates from RSG pulsation (M. D. Soraisam et al. 2023) and environment analysis (Z. Niu et al. 2023).

During the drafting of this manuscript, B. Hsu et al. (2024) presented their analysis of SN 2023ixf. Using the RSG model grid from D. Hiramatsu et al. (2021), they found that, by varying the explosion energy, models with $M_{\rm Henv} \sim 3\,M_{\odot}$ can produce light curves that well match with observation, despite the fact that $M_{\rm ZAMS}$ varies from 15 to $22.5\,M_{\odot}$. They further use the pre-SN variability of the progenitor to constrain the properties of the progenitor and conclude that RSG models with $M_{\rm ZAMS} > 17\,M_{\odot}$, $R > 950\,R_{\odot}$, and $M_{\rm Henv} < 3\,M_{\rm Henv}$ can explain the pulsation period (~ 1100 days) as well as reproduce the observed multiband light curve of SN 2023ixf. From their Table 1, the favored models have helium core mass $M_{\rm He\ core} > 5.5\,M_{\odot}$, or $M_{\rm ZAMS} > 18.3\,M_{\odot}$ using the $M_{\rm ZAMS}$–$M_{\rm He\ core}$ relation of `Kepler` RSG models (T. Sukhbold et al. 2016). This value is not favored by the nebular spectroscopy analysis presented in L. Ferrari et al. (2024) and this work. However, the [O I] flux is mainly determined by the oxygen mass in the ejecta. Given the same $M_{\rm He\ core}$, `MESA` seems to predict systematically lower carbon-oxygen core mass ($M_{\rm CO\ core}$) than `Kepler` (see the comparison between D. Temaj et al. 2024 and T. Sukhbold et al. 2016), possibly due to

different treatments on the microphysics of the two codes. Using the $M_{\rm He\ core}$–$M_{\rm CO\ \ core}$ presented in D. Temaj et al. (2024), the models from B. Hsu et al. (2024) with $M_{\rm ZAMS} = 17.5$–$18.0\,M_{\odot}$ will have $M_{\rm CO\ core} = 3.65$–$3.90\,M_{\odot}$, translating into $M_{\rm ZAMS} = 16.6$–$17.3\,M_{\odot}$ for `Kepler` models. Given the uncertainties in the nebular spectroscopy model and direct interpolation, we consider this $M_{\rm ZAMS}$ range to match our estimation. However, the other two models (20.5M_eta1.5_alpha1.5 and 21.5M_eta1.5_alpha1.5) can be ruled out. Combining with nebular spectroscopy analysis, we narrow down the $M_{\rm ZAMS}$ range from B. Hsu et al. (2024) to 17.5–$18.0\,M_{\odot}$. In conclusion, the $M_{\rm ZAMS}$ of the SN 2023ixf progenitor should be around 15.0–$18.0\,M_{\odot}$.

Acknowledgments

The authors would like to thank the anonymous reviewer for the comments that helped to improve the manuscript Q.F. acknowledges support from JSPS KAKENHI grant 24KF0080. T.J.M. is supported by the Grants-in-Aid for Scientific Research of the Japan Society for the Promotion of Science (JP20H00174, JP21K13966, JP21H04997). K.M. acknowledges support from JSPS KAKENHI grants JP20H00174, JP24H01810, and 24KK0070. K.M. and H.K. are supported by the JSPS bilateral program between Japan and Finland (JPJSBP120229923). T.M. acknowledges support from the Hakubi project at Kyoto University.

Software: `MESA` (B. Paxton et al. 2011, 2013, 2015, 2018, 2019; A. S. Jermyn et al. 2023); `STELLA` (S. I. Blinnikov et al. 1998; S. Blinnikov et al. 2000; S. I. Blinnikov et al. 2006) `SciPy` (P. Virtanen et al. 2020); `NumPy` (C. R. Harris et al. 2020); Astropy (Astropy Collaboration et al. 2013, 2018); `Matplotlib` (J. D. Hunter 2007).

ORCID iDs

Qiliang Fang https://orcid.org/0000-0002-1161-9592
Takashi J. Moriya https://orcid.org/0000-0003-1169-1954
Lucía Ferrari https://orcid.org/0009-0000-6303-4169
Keiichi Maeda https://orcid.org/0000-0003-2611-7269
Gaston Folatelli https://orcid.org/0000-0001-5247-1486
Keila Y. Ertini https://orcid.org/0000-0001-7251-8368
Hanindyo Kuncarayakti https://orcid.org/0000-0002-1132-1366
Jennifer E. Andrews https://orcid.org/0000-0003-0123-0062
Tatsuya Matsumoto https://orcid.org/0000-0002-9350-6793

References

Andrews, J. E., Sand, D. J., Valenti, S., et al. 2019, ApJ, 885, 43
Astropy Collaboration, Price-Whelan, A. M., Sipőcz, B. M., et al. 2018, AJ, 156, 123
Astropy Collaboration, Robitaille, T. P., Tollerud, E. J., et al. 2013, A&A, 558, A33
Blinnikov, S., Lundqvist, P., Bartunov, O., et al. 2000, ApJ, 532, 1132
Blinnikov, S. I., Eastman, R., Bartunov, O. S., et al. 1998, ApJ, 496, 454
Blinnikov, S. I., Röpke, F. K., Sorokina, E. I., et al. 2006, A&A, 453, 229
Berger, E., Keating, G. K., Margutti, R., et al. 2023, ApJL, 951, L31
Bersten, M. C., Orellana, M., Folatelli, G., et al. 2024, A&A, 681, L18
Bostroem, K. A., Pearson, J., Shrestha, M., et al. 2023, ApJL, 956, L5
Burrows, A., & Vartanyan, D. 2021, Natur, 589, 29
Burrows, A., Wang, T., & Vartanyan, D. 2024, ApJL, 964, L16
Cardelli, J. A., Clayton, G. C., & Mathis, J. S. 1989, ApJ, 345, 245
Chandra, P., Maeda, K., Chevalier, R. A., et al. 2023, ATel, 16073, 1
Chugai, N. N., Fabrika, S. N., Sholukhova, O. N., et al. 2005, AstL, 31, 792
Dessart, L., & Hillier, D. J. 2019, A&A, 625, A9
Dessart, L., & Hillier, D. J. 2020, A&A, 642, A33
Dessart, L., Hillier, D. J., Li, C., & Woosley, S. 2012, MNRAS, 424, 2139
Dessart, L., Hillier, D. J., Waldman, R., & Livne, E. 2013, MNRAS, 433, 1745
Dong, Y., Sand, D. J., Valenti, S., et al. 2023, ApJ, 957, 28
Ercolino, A., Jin, H., Langer, N., & Dessart, L. 2024, A&A, 685, A58
Fang, Q., Maeda, K., Kuncarayakti, H., & Nagao, T. 2024, NatAs, 8, 111
Fang, Q., Maeda, K., Kuncarayakti, H., Sun, F., & Gal-Yam, A. 2019, NatAs, 3, 434
Fang, Q., Maeda, K., Kuncarayakti, H., et al. 2022, ApJ, 928, 151
Fang, Q., Maeda, K., Ye, H., et al. 2024, arXiv:2404.01776
Farmer, R., Fields, C. E., Petermann, I., et al. 2016, ApJS, 227, 22
Ferrari, L., Folatelli, G., Ertini, K., Kuncarayakti, H., & Andrews, J. E. 2024, A&A, 687, L20
Fransson, C., & Chevalier, R. A. 1989, ApJ, 343, 323
Fuller, J., & Tsuna, D. 2024, OJAp, 7, 47
Goldberg, J. A., Bildsten, L., & Paxton, B. 2019, ApJ, 879, 3
Goldberg, J. A., Bildsten, L., & Paxton, B. 2020, ApJ, 891, 15
Grefenstette, B. W., Brightman, M., Earnshaw, H. P., et al. 2023, ApJL, 952, L3
Gvaramadze, V. V., Menten, K. M., Kniazev, A. Y., et al. 2014, MNRAS, 437, 843
Harris, C. R., Millman, K. J., van der Walt, S. J., et al. 2020, Natur, 585, 357
Hiramatsu, D., Howell, D. A., Moriya, T. J., et al. 2021, ApJ, 913, 55
Hiramatsu, D., Tsuna, D., Berger, E., et al. 2023, ApJL, 955, L8
Hosseinzadeh, G., Farah, J., Shrestha, M., et al. 2023, ApJL, 953, L16
Hsu, B., Smith, N., Goldberg, J. A., et al. 2024, arXiv:2408.07874
Hunter, J. D. 2007, CSE, 9, 90
Itagaki, K. 2023, Transient Name Server Discovery Report, 2023-1158
Jacobson-Galán, W. V., Dessart, L., Margutti, R., et al. 2023, ApJL, 954, L42
Jencson, J. E., Pearson, J., Beasor, E. R., et al. 2023, ApJL, 952, L30
Jerkstrand, A. 2017, Handbook of Supernovae (Berlin: Springer), 795
Jerkstrand, A., Fransson, C., Maguire, K., et al. 2012, A&A, 546, A28
Jerkstrand, A., Smartt, S. J., Fraser, M., et al. 2014, MNRAS, 439, 3694
Jermyn, A. S., Bauer, E. B., Schwab, J., et al. 2023, ApJS, 265, 15
Kasen, D., & Woosley, S. E. 2009, ApJ, 703, 2205
Kilpatrick, C. D., Foley, R. J., Jacobson-Galán, W. V., et al. 2023, ApJL, 952, L23
Kippenhahn, R., Ruschenplatt, G., & Thomas, H.-C. 1980, A&A, 91, 175
Kumar, B., Pandey, S. B., Eswaraiah, C., & Kawabata, K. S. 2016, MNRAS, 456, 3157
Kuncarayakti, H., Folatelli, G., Maeda, K., et al. 2020, ApJ, 902, 139
Leonard, D. C., & Filippenko, A. V. 2001, PASP, 113, 920
Leonard, D. C., Filippenko, A. V., Ganeshalingam, M., et al. 2006, Natur, 440, 505
Levesque, E. M., Massey, P., Olsen, K. A. G., et al. 2005, ApJ, 628, 973
Li, G., Hu, M., Li, W., et al. 2024, Natur, 627, 754
Liu, C., Chen, X., Er, X., et al. 2023, ApJL, 958, L37
Lundquist, M., O'Meara, J., & Walawender, J. 2023, Transient Name Server AstroNote, 2023-160
Maeda, K., Kawabata, K., Mazzali, P. A., et al. 2008, Sci, 319, 1220
Maeda, K., Nakamura, T., Nomoto, K., et al. 2002, ApJ, 565, 405
Maeda, K., Nomoto, K., Mazzali, P. A., et al. 2006, ApJ, 640, 854
Martinez, L., Bersten, M. C., Anderson, J. P., et al. 2020, A&A, 642, A143
Martinez, L., Bersten, M. C., Folatelli, G., et al. 2024, A&A, 683, A154
Mazzali, P. A., Kawabata, K. S., Maeda, K., et al. 2005, Sci, 308, 1284
Mereminskiy, I. A., Lutovinov, A. A., Sazonov, S. Y., et al. 2023, ATel, 16065, 1
Messineo, M., & Brown, A. G. A. 2019, AJ, 158, 20
Milisavljevic, D., Fesen, R. A., Gerardy, C. L., et al. 2010, ApJ, 709, 1343
Modjaz, M., Kirshner, R. P., Blondin, S., et al. 2008, ApJL, 687, L9
Moriya, T., Tominaga, N., Blinnikov, S. I., Baklanov, P. V., & Sorokina, E. I. 2011, MNRAS, 415, 199
Moriya, T. J., & Singh, A. 2024, PASJ, 76, 1050
Morozova, V., Piro, A. L., Renzo, M., et al. 2015, ApJ, 814, 63
Morozova, V., Piro, A. L., & Valenti, S. 2018, ApJ, 858, 15
Nagao, T., Cikota, A., Patat, F., et al. 2019, MNRAS, 489, L69
Nagao, T., Maeda, K., Mattila, S., et al. 2024, A&A, 687, L17
Nagao, T., Patat, F., Cikota, A., et al. 2024, A&A, 681, A11
Neustadt, J. M. M., Kochanek, C. S., & Smith, M. R. 2024, MNRAS, 527, 5366
Niu, Z., Sun, N.-C., Maund, J. R., et al. 2023, ApJL, 955, L15
Panjkov, S., Auchettl, K., Shappee, B. J., et al. 2024, PASA, 41, e059
Paxton, B., Bildsten, L., Dotter, A., et al. 2011, ApJS, 192, 3
Paxton, B., Cantiello, M., Arras, P., et al. 2013, ApJS, 208, 4
Paxton, B., Marchant, P., Schwab, J., et al. 2015, ApJS, 220, 15
Paxton, B., Schwab, J., Bauer, E. B., et al. 2018, ApJS, 234, 34

Paxton, B., Smolec, R., Schwab, J., et al. 2019, ApJS, 243, 10
Pledger, J. L., & Shara, M. M. 2023, ApJL, 953, L14
Qin, Y. -J., Zhang, K., Bloom, J., et al. 2024, MNRAS, 534, 271
Ransome, C. L., Villar, V. A., Tartaglia, A., et al. 2024, ApJ, 965, 93
Riess, A. G., Yuan, W., Macri, L. M., et al. 2022, ApJL, 934, L7
Soraisam, M. D., Bildsten, L., Drout, M. R., et al. 2018, ApJ, 859, 73
Soraisam, M. D., Szalai, T., Van Dyk, S. D., et al. 2023, ApJ, 957, 64
Sukhbold, T., Ertl, T., Woosley, S. E., et al. 2016, ApJ, 821, 38
Sun, N.-C., Maund, J. R., Crowther, P. A., Fang, X., & Zapartas, E. 2021, MNRAS, 504, 2253
Schlafly, E. F., & Finkbeiner, D. P. 2011, ApJ, 737, 103
Shrestha, M., DeSoto, S., Sand, D. J., et al. 2024, arXiv:2410.08199
Singh, A., Teja, R. S., Moriya, T. J., et al. 2024, ApJ, 975, 132
Smith, N., Pearson, J., Sand, D. J., et al. 2023, ApJ, 956, 46
Taubenberger, S., Valenti, S., Benetti, S., et al. 2009, MNRAS, 397, 677
Teja, R. S., Singh, A., Basu, J., et al. 2023, ApJL, 954, L12
Temaj, D., Schneider, F. R. N., Laplace, E., et al. 2024, A&A, 682, A123
Utrobin, V. P., & Chugai, N. N. 2019, MNRAS, 490, 2042
Utrobin, V. P., Chugai, N. N., Andrews, J. E., et al. 2021, MNRAS, 505, 116
van Baal, B. F. A., Jerkstrand, A., Wongwathanarat, A., et al. 2023, MNRAS, 523, 954
Van Dyk, S. D., Srinivasan, S., Andrews, J. E., et al. 2024, ApJ, 968, 27
Vasylyev, S. S., Yang, Y., Filippenko, A. V., et al. 2023, ApJL, 955, L37
Vasylyev, S. S., Yang, Y., Patra, K. C., et al. 2024, MNRAS, 527, 3106
Virtanen, P., Gommers, R., Oliphant, T. E., et al. 2020, NatMe, 17, 261
Wang, L., & Wheeler, J. C. 2008, ARA&A, 46, 433
Xiang, D., Mo, J., Wang, L., et al. 2024, SCPMA, 67, 219514
Yamanaka, M., Fujii, M., & Nagayama, T. 2023, PASJ, 75, L27
Yoon, S.-C., & Cantiello, M. 2010, ApJL, 717, L62
Zimmerman, E. A., Irani, I., Chen, P., et al. 2024, Natur, 627, 759